HHS Public Access

Author manuscript

Methods Appl Fluoresc. Author manuscript; available in PMC 2018 March 28.

Published in final edited form as:

Methods Appl Fluoresc. ; 6(2): 024003. doi:10.1088/2050-6120/aa9949.

Conversion of Isotropic Fluorescence into a Long-Range Non-Diverging Beam

Douguo Zhang[1,*], **Liangfu Zhu**[1], **Junxue Chen**[2,*], **Ruxue Wang**[1], **Pei Wang**[1], **Hai Ming**[1], **Ramachandram Badugu**[3], **Mary Rosenfeld**[3], **Qiwen Zhan**[4], **Cuifang Kuang**[5], **Xu Liu**[5], and **Joseph R. Lakowicz**[3,*]

[1]Institute of Photonics, Department of Optics and Optical Engineering, University of Science and Technology of China, Hefei, Anhui, 230026, China

[2]School of Science, Southwest University of Science and Technology, Mianyang, Sichuan 621010, China

[3]Center for Fluorescence Spectroscopy, Department of Biochemistry and Molecular Biology University of Maryland School of Medicine, 725 West Lombard St., Baltimore, MD 21201, USA

[4]Department of Electro-Optics and Photonics, University of Dayton, 300 College Park, Dayton, OH, 45469-2951 USA

[5]State Key Laboratory of Modern Optical Instrumentation, College of Optical Science and Engineering, Zhejiang University, Hangzhou 310027, China

Abstract

Fluorescent samples typically emit isotropically in all directions. As a result large lenses and other optical components are needed to capture a significant fraction of the emission, and complex confocal microscopes are required for high resolution focal-plane imaging. Complex optical systems are necessary for manipulation of light propagating in free-space. All propagating light is affected to some extent by surfaces, obstacles or apertures resulting in diffraction. Even the most highly collimated laser beams expand with distance from the source. This expansion is described by Rayleigh range $Z_R = \pi\omega^2_0/\lambda_0$, where ω_0 is the most narrow beam waist size and λ_0 as the free-space wavelength. The value of Z_R is the distance over which a Gaussian beam increases its cross-sectional area by a factor of two. The importance of diffraction can be understood by considering a 500 nm plane wave incident on an opaque mask with a 2 micron diameter hole. Even for this seemingly favorable case, with ω_0 4-fold larger than the wavelength, Z_R = 25 microns, showing that light passing through the 2 micron aperture is diffracted and quickly diverges with distance, and the beam area expands 2-fold in 50 λ_0.

Bessel beams have remarkable property of being able to travel long distances, over 1000 times the wavelength, without diverging into a wider beams. The diameter of the beam can be diffraction limited over the entire distance. To be specific, a 2 micron diameter beam retains a 2 micron diameter for long distance, and a point source results in a Bessel beam with a diameter comparable to the diffraction-limited resolution of the optics. In all previous reports the Bessel beams were

Correspondence and requests for materials should be addressed to D.G. Zhang. (dgzhang@ustc.edu.cn) or J. X. Chen (cjxueoptics@163.com) or J.R. Lakowicz (JLakowicz@som.umaryland.edu).

formed by an incident light source, typically with plane-wave illumination on a circular aperture. It was not known if Bessel beams could form using an incoherent fluorescent light source, especially within near-field distances from surface where plane waves have not yet formed. Herein we demonstrate transformation of the emission from fluorescent polystyrene spheres into non-diverging beams which propagate up to 130 mm (13 cm) along the optical axis with a constant diameter. This is accomplished using a planar metal film, with no nanoscale features in the X–Y plane, using surface plasmon-coupled emission. Furthermore, using samples which contain many fluorescent polystyrene spheres in the field-of-view, we demonstrate that an independent Bessel beam can be generated from any location on the metal film. The extremely long non-diffracted propagation distances offer new opportunities in fluorescence sensing and imaging.

Graphical Abstract

The generally regarded incoherent fluorescence emission could be converted to nondiffracting form. Fluorescence Bessel-like beams could be obtained by using a 4f imaging system to convert the directional emission of surface plasmon-coupled emission. Multiple Bessel beams could be generated at the same time which would have potential application in fluorescence imaging.

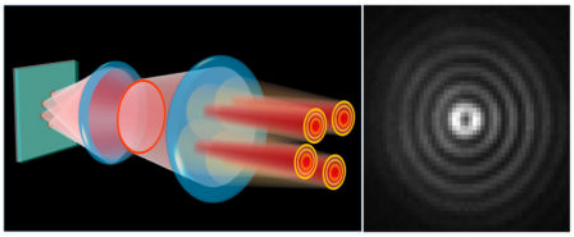

Introduction

Fluorescence imaging of surfaces is widely used in biological research. Microwell plates with macroscopic dimensions are used for clinical assays, drug discovery [12], and printed arrays are used in genomics and proteomics [3–4]. Most microwell plates and spotted array imagers use sequential point-by-point (PbP) measurements to obtain the images because it is difficult and expensive to create optical components for wide-field imaging of large areas. Cell imaging requires the highest possible spatial resolution and diffraction-limited optics. Research microscopes often use confocal optics to select emission from only the focal plane of the objective [5–6]. Laser scanning confocal microscopes provide diffraction-limited images with 300 nm resolution in the (X–Y) plane of the sample and 1 μm along the Z axis. Higher spatial resolution to about 50 nm is possible using super-resolution imaging [7–8], with various approaches such as stimulated emission depletion (STED) or stochastic optical reconstruction microscopy (STORM) [9–10], but this require added complexity to the optics and additional laser light sources. The high spatial resolution and magnification needed for cell imaging results in a very limited field-of-view (FoV), which is not adequate for applications such as pathology where entire slides need to be examined [11–12] or imaging of tissue samples [13–14].

During the past four decades there has been enormous progress in electronic devices and computers. However, there has not been a comparable decrease in cost, complexity or size of

optical devices. Compared to electronics, optical technology has progressed slowly in the past 140 years since the diffraction limit was recognized. Improvements in optics have been incremental and based on the classical theory of refraction and improved materials and manufacturing. The static situation is rapidly changing with the discovery of photonic band gaps (PBG) [15–16], surface-bound states on dielectrics or metallic structures [17–19] and the application of classical electrodynamics (Maxwell's equations) to nanoscale structures [20–21], all of which are providing new methods to manipulate the flow of optical energy using nano-scale structures.

Many laboratories have applied the emerging knowledge of nano-optics to fluorescence imaging and sensing [22–25]. These efforts have resulted in new concepts for fluorescence probes and imaging which depend on the interactions of fluorophores with particles and surfaces. Planar metallic surfaces were found to convert spatially isotropic emission into a cone of emission around the surface normal (Z-axis) [26–28], which is called surface plasmon-coupled emission (SPCE). This is a remarkable phenomenon because it demonstrated that optical energy, in this case fluorescence, radiates with an angular distribution and polarization determined by the metallic structure. This basic concept has been used to obtain fluorescence beaming normal to the surface, and has been obtained using metallic nanorings [29–30]. However, these structures require top-down nanofabrication which is not practical for large area disposable slides. The potential for alternative optical configurations was greatly increased in 1987 with the discovery of Bessel beams which can propagate long distances without an increase in beam diameter [31–32]. These reports used plane-wave incident light to create the Bessel beams. It would be valuable if fluorescence, which occurs in all directions and is not a plane wave at short distances, could be used to create long-range Bessel beams. In the present paper we report conversion of the isotropic emission from a fluorescent polystyrene sphere (FPS) into a narrow beam which propagates up to 130 mm along the Z-axis, while maintaining a constant diameter which is close to the diffraction limit. This long-range fluorescence beaming was accomplished using only a continuous planar metal (Ag) film on a glass substrate. We found the SPCE cone-of-emission could be used as equivalent to a circular aperture in an opaque structure to obtain fluorescent non-diverging Bessel beams. Metal-coated slides with multiple FPS in the field-of-view resulted in multiple Bessel beams and an image of the FPS location, suggesting the use of Bessel beams for imaging.

Introduction to Bessel Beams

Diffraction is a phenomenon originating from the wave nature of light and has implications for the performance of all optical systems. This effect occurs when any wave-front is obstructed in some manner, and thus present in instruments with limited apertures. Even a well collimated laser beam will expand as it propagates over long distances. Durnin et al. [31–32] showed that these effects can be counter balanced by the use of intersecting beams of light. Optical beams of Bessel-type profiles can propagate indefinitely without change of their transverse width or intensity. A true Bessel beam has an infinite number of concentric rings, and with an infinite propagation distance would carry infinite power. Hence, a more accurate term is Bessel-like beams. In practice, the non-diffracting distance that a Bessel-

like beam can propagate without significant alteration in their transverse profiles is limited by the aperture of the optical system.

The phenomenon of Bessel beams (BBs) is not mentioned in some of the most widely used textbooks on optics except in the context of focal plane (FP) imaging [32–34], so we briefly review formation of Bessel beams from an incident plane wave [35–38]. Bessel beams can be formed using an axicon, which is a prism shaped like a flattened cone. A parallel incident light on the back of the axicon is directed towards the center and overlaps along the Z-axis. The intersecting beams produce a Bessel-type profile along the Z-axis (Figure 1). A more intuitive approach is to use an optical mask with a circular aperture in the objective back focal plane (BFP) (Figure 1). This approach is not efficient because most of the incident light is blocked by the mask and only a small fraction passes through the aperture. In either case the beam profile is described by a zero-order Bessel function (J_o) which consists of a central bright spot surrounded by concentric rings. Other more efficient methods of creating Bessel-like beam, including those using holographic techniques [39–41] that imprint the appropriate phase of a Bessel beam onto an incoming Gaussian beam. To the best of our knowledge, there have been no reports on conversion of fluorescence, instead of the incident light, to create a Bessel-like beam. We refer to Bessel beams created by fluorescence as non-diffracted fluorescence (NDF).

Methods and Results

Figure 2a presents the schematic configuration of the experimental setup for formation of a non-diffracting fluorescence beam. The apparatus is based on an inverted total internal reflection fluorescence (TIRF) microscope with a high numerical aperture (N.A) objective (60 X, N.A 1.49,). An isolated 40 nm diameter fluorescent polystyrene sphere (FPS) is used as a point source, with an emission maximum of 555 nm (Figure 2B). The fluorescent bead or beads are spin-coated on a silver film (of 45 nm thickness) coated coverslip and illuminated by a laser beam at 532 nm. The P-polarized laser beam was focused on the BFP objective at the surface plasmon resonance (SPR) angle and generates the SPs at the Ag/Air interface. Excitation of the FPS is accomplished by the evanescent field.

Excited fluorophores within the near-field distances from the silver film can couple with surface plasmons on Ag/Air interface by near-field dipole-metal interactions. These plasmons radiate into a higher refractive index medium (such as the glass substrate) with a narrow angular distribution which is known as SPCE [28], resulting in a bright circular ring on the back focal plane (BFP) of the collection objective [42]. In contrast to an opaque mask with a circular aperture, the system is more efficient because no mechanical annular ring is needed with SPCE and all the coupled light can be used to create the Bessel beams. The coupled fluorescence forms a ring on the BFP of the objective. With a conventional infinity-corrected 4f microscope system, the BFP of the objective is overlapped with one of the focal planes of the tube lens (or named Fourier lens), with a focal length of 300 mm. The fluorescence ring will be transformed to waves propagating on a converging cone. We hypothesized that a diffraction-free Bessel beam could be created by the converging cone of coupled emission within the overlapping region between the tube lens and the FFP (Figure 2a).

Results

We used a scientific CMOS camera (Andor) to record the transverse intensity distribution along the Z axis. The front focal plane (FFP) is considered to be at Z = 0. Distances before the FFP are considered to be negative (Z < 0), and those beyond the FFP are considered to be positive (Z > 0). The tube lens with a focal length of 300 mm is located at Z = −300 nm.

The transverse intensity distribution was measured at 10 mm intervals along the Z-axis (Figure 3a). The image size is 51 pixels × 51 pixels and pixel size of the sCMOS is 6.5 μm. The generated beam consists of a series of uniformly-spaced concentric rings and which propagates more than one hundred millimeters (130 mm in this case) without noticeable change of beam width or intensity, which can only occur if the emission formed a Bessel beam. According to the schematic drawn in Figure 2, the superposition region of plane waves ends after the tube lens ends at the imaging plane (FFP plane on Figure 2a) of the 4f system, indicating that the beam will disappear at this location. This prediction was confirmed by our measurements and no image was observed beyond Z = −10 or 20 nm, where a Bessel beam was not observed. For comparisons, when the fluorescent bead was placed on a bare glass substrate without the silver film, then there is no Bessel beam or directional fluorescence emission at Z > or < 0. The fluorescence images captured at different *Z* positions (Figure 3d) show that the emission pattern diverges greatly with the decreasing of Z (the camera moves towards the tube lens) and did not display any non-diffracting propagation. The center cross-section of transverse pattern recorded at −20mm was chosen for a more detailed analysis. A lone scan across the image shows a doughnut pattern with a main lobe and side lobes. The doughnut pattern, with a low center intensity, has been reported previously for FP images of SPCE [43–44], but there are no previous reports on constant doughnut and/or Bessel beam images along the Z-axis. It is possible that Bessel beams were present in these experiments [43–44] but were not observed because the goal was to measure the point-spread function at the FP. Figure 3c shows the measured main lobe width and side lobe period of the transverse intensity distribution at different propagation distances (*Z*), after the tube lens with steps of 5 mm. The main lobe width remains unchanged (about 11 pixels or 71.5 μm), which shows the beam is not diffracting or diverging. The period of the concentric rings (side lobes) is generally 4 pixels (26 μm).

The doughnut hole pattern (Figure 3) is surprising because the classical image of Bessel beams has a high central peak (Figure 1), but the images in Figure 3a are consistent with a first order Bessel beam (J_1), which is expected for radially-polarized incident light [45]. The polarization state of the coupled emission was observed in the BFP and at a distance Z = −20 mm. The BFP images at different polarizer orientations indicate radial or p-polarized emission at all angles around the Z-axis (Figure 4a–e). The radially polarization is also present in the BB images (Figures 3f–j). This radial polarization is thought to be the origin of the doughnut hole images of the BB. This result confirms the Bessel beams can be created by an incoherent fluorescent source and display the same optical properties as Bessel beams created by plane wave or Gaussian incident light.

Simulations of Bessel Beams

To confirm and further understand the experimental results, we performed simulations of coupled fluorescence from a point source on a metal film using the same geometry used for the experiments (Figure 5). A dipole placed at a distance d (here d = 0 nm) away from the metal film (thickness is *t*) is used to mimic the fluorescent bead shown in Figure 2. The silver film (at a wavelength of 555 nm, the refractive index of silver is n = 0.123+3.380*1i) has the same thickness *t* = 45 nm as on a glass substrate (the refractive index of glass is n = 1.515). Simulated emission from the dipole is then calculated for the 4f optical system. The point dipole emits at a longer wavelength (555 nm) than the excitation wavelength (532 nm), and the excited state fluorophore orientation is excited by the SP field and is expected to be essentially random. According to vector diffraction theory [46–48], the field in the image space of the tube lens is given by:

$$\boldsymbol{E}_4(r,\varphi,z)=\frac{-ik_4}{2\pi}\int\int_{\Omega}\boldsymbol{E}_4^{'}\sin\theta_4\exp\left[ik_4 r\sin\theta_4\cos(\phi-\varphi)\right]\exp\left[ik_4 z\cos\theta_4\right]d\theta_4 d\phi, \quad (1)$$

where $\boldsymbol{E}_4^{'}$ is the electric field near the tube lens, which can be obtained from the generalized Jones matrix (Supplemental material, part A). Then, the electric field components of $\boldsymbol{E}_4$ emitted by a dipole $\vec{\boldsymbol{p}} = (p_x, p_y, p_z)$ can be obtained.

$$\begin{aligned}
E_{4,r}&=\frac{-jk_4}{2}\left\{(p_x\cos\varphi+p_y\sin\varphi)\left[K_0^I+K_2^I\right]-2ip_zK_1^I\right\}\\
E_{4,\varphi}&=\frac{-jk_4}{2}\left\{(-p_x\sin\varphi+p_y\cos\varphi)\left[K_0^I-K_2^I\right]\right\}\\
E_{4,z}&=\frac{-jk_4}{2}\left\{2i\,(p_x\cos\varphi+p_y\sin\varphi)\,K_1^{II}-2p_zK_0^{II}\right\}
\end{aligned} \quad (2)$$

where

$$\begin{aligned}
K_0^I&=\int_0^{\sigma}\sqrt{\frac{\cos\theta_4}{\cos\theta_3}}\,(\tau_s+\tau_p\cos\theta_1\cos\theta_4)\,J_0\,(k_4r\sin\theta_4)\,\sin\theta_4\exp(ik_4z\cos\theta_4)d\theta_4\\
K_1^I&=\int_0^{\sigma}\sqrt{\frac{\cos\theta_4}{\cos\theta_3}}\,\tau_p\sin\theta_1\cos\theta_4J_1\,(k_4r\sin\theta_4)\,\sin\theta_4\exp(ik_4z\cos\theta_4)d\theta_4\\
K_2^I&=\int_0^{\sigma}\sqrt{\frac{\cos\theta_4}{\cos\theta_3}}\,(\tau_s-\tau_p\cos\theta_1\cos\theta_4)\,J_2\,(k_4r\sin\theta_4)\,\sin\theta_4\exp(ik_4z\cos\theta_4)d\theta_4\\
K_0^{II}&=\int_0^{\sigma}\sqrt{\frac{\cos\theta_4}{\cos\theta_3}}\,\tau_p\sin\theta_1\sin\theta_4J_0\,(k_4r\sin\theta_4)\,\sin\theta_4\exp(ik_4z\cos\theta_4)d\theta_4\\
K_1^{II}&=\int_0^{\sigma}\sqrt{\frac{\cos\theta_4}{\cos\theta_3}}\,\tau_p\cos\theta_1\sin\theta_4J_1\,(k_4r\sin\theta_4)\,\sin\theta_4\exp(ik_4z\cos\theta_4)d\theta_4
\end{aligned} \quad (3)$$

The terms τ_s and τ_p are the three-layer Fresnel coefficient for P-polarized and S-polarized plane waves, respectively. θ_1, θ_3, and θ_4, are the semi-angle in the medium 1, 3 and 4, respectively. The relationship among them can be established by using the Abbe sine condition. k_4 is the wavenumber in the medium 4. Considering the fact that a single bead contains emitters of different dipole orientations, the intensity in the image space is integrated over all polar and azimuthal directions, which is given as:

$$I \propto \int_0^{\pi}\int_0^{2\pi} \left(|E_{4,r}|^2+|E_{4,\varphi}|^2+|E_{4,z}|^2\right) \sin\theta_d d\theta_d d\phi_d \quad (4)$$

The intensity patterns at different distances (positions Z) in the image space are calculated based on Eq. (4) (shown in Fig. 6(a)). The simulated transverse intensity distributions (on the X–Y plane) demonstrate almost the same distributions at distances along the Z-axis for Z < 130 nm. As the recording plane moves toward the FFP along the -Z axis, converging circular rings patterns can be observed. This effect can be understood as due to a decreasing area of beam overlap as Z approaches zero (Figure 2). Moreover, as the recording plane further moves into the positive Z regions (such as Z = 20 mm), diverging patterns are observed and the Bessel beam rapidly disappears. Normalized intensities extracted from the transverse patterns at (Figure 6b) gives simulated main lobe width and side lobes intensities which are good agreement with that shown in Figure 3b. However, the calculated main lobe width and side lobes period (Figure 5c) demonstrate the periodic oscillation along the propagation direction. The oscillation amplitude is less than one pixel, which cannot be distinguished in the experimental results (Figure 3c).

The periodic oscillation can be understood along the Z-axis as follows. Figure 7 shows the non-diffraction property originates from the fluorescence ring at the back focal plane of objective, which is Z-polarized (perpendicular to the glass substrate). The intensity patterns in the image space for the dipole with X and Z orientations were also simulated and shown in the Supplementary Figures 1 and 2, which indicates that the constant intensity profile and non-diffraction property is mainly related to dipoles with Z-orientation. The electric field in Eq. (4) can be simplified by just considering the role of dipole with Z-orientation. Moreover, the contribution of $E_{4,z}$ to the intensity pattern can be ignored due to the low numerical aperture of the tube lens. The intensity in the image space of tube lens can be obtained as:

$$I \propto \left| \frac{k_4}{2} \int_0^{\sigma} \sqrt{\frac{\cos\theta_4}{\cos\theta_3}} \tau_p \sin\theta_1 \sin 2\theta_4 J_1\left(k_4 r \sin\theta_4\right) \exp\left(ik_4 z \cos\theta_4\right) d\theta_4 \right|^2 . \quad (5)$$

The Fresnel transmission coefficient τ_p achieves the maximum value at the excitation angle of the SPs on the metal/air interface, which plays a key role in determining the intensity distribution in Eq. (5). According to the Abbe sine condition, the excitation angle of SPs can be expressed as:

$$n_{spp}=n_3\sin\theta_3=M\cdot n_4\sin\theta_4 \quad (6)$$

where M is the overall magnification factor of the 4f imaging system, n_{spp} is the mode effective refractive index of SPs. Therefore, the first zero point and intervals between other zero points of the Bessel function $J_1(k_4 r\sin\theta_4)$ determine the main lobe width and the side lobe period of the transverse intensity distribution. The main lobe width and the side lobe period can be found as:

$$w_{main\ lobe}=2*\frac{3.8317M}{k_0 n_{spp}},\ P_{side\ lobe}\approx\frac{3.15M}{k_0 n_{spp}} \quad (7)$$

According to the Fresnel formula, the mode effective refractive index of SPs (on the Ag/Air interface with emission wavelength at 555 nm.) is about 1.048. The magnification coefficient M of the *4f* imaging system is about 100. Then, the main lobe width and side lobe period of the transverse patterns are estimated as 64.6 μm and 26.5 μm, respectively, which coincide with the experimental results shown in Figure 3c and also are consistent with the simulated results shown in Figure 5b. Given the estimated magnification of 100 the Bessel beams and rings originate from regions with dimensions of 646 nm and 265 nm, respectively. These dimensions are consistent with the reported 2-fold decrease in spatial resolution for SPCE microscopy as compared to slides without metal films [43–44].

Furthermore, the transmission coefficient τ_p determines a certain angular plane wave spectrum width due to the absorption of the silver film, corresponding to the width of the fluorescence ring on the pupil plane of the objective. In general, the angular spectrum width for the excitation of SPs is very small, Eq. (4) can be further simplified as:

$$I\propto A(k_4,\theta_0,r)\left|\int_{\theta_0-\Delta\theta/2}^{\theta_0+\Delta\theta/2}\tau_p(\theta_{30},\Delta\theta)\exp(ik_4 z\cos\theta_4)\,d\theta_4\right|^2, \quad (8)$$

Where $A(k_4,\theta_0,r)=k_4^2\sin^2\theta_{40}\cos^3\theta_{40}\sin^2\theta_{10}J_1^2(k_4 r\sin\theta_{40})/\cos\theta_{30}$, θ_{i0} (i = *1, 3, 4*) and $\Delta\theta$ corresponds to the excitation angle and the angular plane wave spectrum width of SPs, respectively. Consequently, the Bessel beam will be modulated by the second term ($\left|\int_{\theta_0-\Delta\theta/2}^{\theta_0+\Delta\theta/2}\tau_p(\theta_{30},\Delta\theta)\exp(ik_4 z\cos\theta_4)\,d\theta_4\right|^2$) in the Eq. (4), giving rise to the oscillation of the main lobe width and side lobe period of NDF along the Z direction.

Removal of the Doughnut Hole and Increase in Spatial Resolution

The use of SPCE in fluorescence microscopy has been discouraged by the doughnut hole pattern which results in a 2-fold decrease in spatial resolution [43–44]. This J_1 distribution occurs when the emission ring has radial polarization, which was demonstrated by the BFP images in Figure 4 where the double headed arrow indicates the polarization direction. The corresponding transverse intensity pattern of the fluorescence at $Z=-20$mm are also measured and presented in Figures 4f–4j. These images clearly verify that the emissions at

the BFP and in the non-diffracted beam are radially polarized. Similar to the previously studied high order Bessel Beams [49–50], the intensity nulls are mainly associated with the phase singularity in the beam. The null center of the diffraction free fluorescence can also be regarded as phase singularity caused by the radially polarization of directional emission. The polarization vectors at diametric positions (180° apart) within the cross-section of the emission pattern have a π phase shift, which determines that the generated beam is Bessel Beam of the first-order. The radially polarized fluorescence can be converted into zero-order NDF, and thereby obtain higher spatial resolution, using a vortex phase plate (VPP) inserted into the optical path as demonstrate in Figure 2a. The VPP is an optical element that has a thickness that increases linearly with the azimuthal angle. The VPP introduces a vortex phase expressed by $e^{i\phi}$ that causes polarization vectors at diametric positions within the cross section to be in phase, leading to constructive interference for the field in the beam center and a bright central spot in the focal plane images [44].

Figure 7 presents the zero-order diffraction free fluorescence after the conversion with a VPP. Figure 7a shows the transvers intensity distribution at different Z positions as labeled in each image. Figure 7b presents the normalized cross-section profile of transvers intensity at position $Z = -20$ mm and Figure 7c presents the statistic main lobe width and side lobe period of the transvers intensity distribution at different propagation distances with steps of 5 mm. In general, the converted zero-order Bessel-like beam inherits the non-diffraction property with the same side lobe period, except the width of the central lobe (or the main lobe of the central spot) is reduced to half of the previous one (first order Bessel-like beam).

We simulated the electric field component of E_4 with the VPP in the optical system (Supplemental Figure 3). The calculated intensity patterns at different Z positions demonstrate the non-diffraction property, which agrees with the experimental results. The intensity patterns for the dipole with X and Z orientations shown in the Supplementary Figures 3 and 4 verify that the zero order diffraction free fluorescence is mainly related to the dipole with Z-orientation.

Similarly, the calculated normalized intensity extracted from the transverse pattern recorded at $Z = -20$ mm and is consistent with the results shown in Figure 7b (not shown). The main lobe width and side lobe period of transverse pattern as a function of propagation distance are shown in Figure 7c. Some oscillation behavior can also be observed in the main lobe width and side lobe width.

Similar to the procedure described above for the first order Bessel beam, the main lobe width and side lobe period of the transverse intensity distribution in the image space are determined by the zero points of the Bessel function $J_0(k_4 r \sin\theta_4)$, which can be written as:

$$w_{main\ lobe} = 2\frac{2.4048M}{k_0 n_{spp}},\ P_{side\ lobe} \approx \frac{3.14M}{k_0 n_{spp}} \quad (9)$$

The main lobe width and side lobe period of the transverse patterns are estimated as 40.5 μm and 26.5 μm, respectively, which agree with the experimental results on Figure 7c.

Considering the 100-fold magnification the initial spot sizes of 403 nm and ring spacing of 265 nm are at the diffraction limit of optical microscopy.

Generation of Multiple Bessel Beams

Bessel beams are rapidly being used in new applications, most of which do not use fluorescence [51–52]. It is important to determine if Bessel beams can be used for fluorescence imaging or sensing at defined locations on a metal film. To test this possibility we used a sample with a continuous thin metal film, and predicted that each location has the potential to generate a diffraction free fluorescence. Figure 8 presents the fluorescence images, at different Z positions as indicated in each panel, with about 25 FPSs in the field-of-view. All the fluorescent beads are on the same silver film and within the field-of-view of the objective. Parallel and independently generated multiple diffraction free beams from beads are clearly observed with a non-diffracting distance of more than a hundred millimeters. The level of background noise increased with more negative Z values. This is due to the non-coherent overlap of emission from different fluorescent beads that is more obvious in the regions close to the tube lens. The background noise reduces the measured non-diffraction range down to 70 mm, which is still long enough for many applications.

Conclusion

Using SPCE and the fluorescent ring at the BFP of the objective, we generated for the first time a non-diverging Bessel beam created by a non-coherent fluorescent point source. Due to the radially polarized emission pattern of the fluorescence ring, the coupled emission has the transverse profile of a first-order Bessel function. The central beam widths are remarkably resistant to the diffractive spreading for distances as long as 130 mm. The first-order beam is close to diffraction limit but the central void results in a 2-fold decrease in effective spatial resolution. The spatial resolution can be increased by changing the first-order beam into a zero-order Bessel beam using a phase plate in the optical path (Figure 2), and thereby approach a diffraction limited beam. Importantly, fluorescence ring can be formed from any location on the silver films. Thus multiple non-diffracting Bessel beams can be generated in a parallel manner from multiple fluorescent beads within field-of-view of the objective. Our work provides a new opportunity for the use of non-diffracting beams that have traditionally been generated from an incident beam, and show that NDF can be obtained from an incoherent source of fluorescence emitters. Bessel beams generated by incident light are finding applications in fluorescence based optical imaging and sensing techniques such as light-sheet microscopy [53–54], optical micromanipulation [54–55], or the use of light beams with curving trajectories [56–57]. An additional property of Bessel beams is their self-healing or self-reconstructing behaviors. If an optical blockage occurs in the Bessel beam it reforms after the block [58–60], so that they can be used for imaging in tissues and scattering media. The present report indicates that all the favorable properties of Bessel beams can be obtained for the coupled emission. To our knowledge Bessel beams are not yet being used for sensing or imaging [61–62] but this is likely to change quickly by the work of the innovative scientists dedicated to these optics.

Supplementary Material

Refer to Web version on PubMed Central for supplementary material.

Acknowledgments

This work was supported by MOST (2013CBA01703, 2016YFA0200601), NSFC (61427818, 11374286), Science and Technological Fund of Anhui Province for Outstanding Youth (1608085J02). This work was also supported by grants from the National Institute of Health (GM107986, EB006521, EB018959 and OD019975). This work was partially carried out at the USTC Center for Micro and Nanoscale Research and Fabrication.

References

1. Mayr LM, Bojanic D. Novel trends in high-throughput screening. Curr Opin Pharm. 2009; 9:580–588.
2. Berg, Brandon, Cortazar, Bingen, Tseng, Derek, Feng, Haydar Ozkan Steve, Wei, Qingshan, Chan, Raymond Y., Burbano, Jordi, Farooqui, Qamar, Lewinski, Michael, Di Carlo, Dino, Garner, Omai B., Ozcan, Aydogan. Cellphone-based hand-held microplate reader for point-of-care testing of enzyme-linked immunosorbent assays. ACS Nano. 2015; 9:7857–7866. [PubMed: 26159546]
3. Heller MJ. DNA microarray technology: Devices, systems, and applications. Annu Rev Biomed Eng. 2002; 4:129–153. [PubMed: 12117754]
4. Lee BH, Nagamune T. Protein microarrays and their applications. Biotech Bioprocess Eng. 2004; 9:69–75.
5. Mondal, PP., Diaspro, A. Fundamentals of Fluorescence Microscopy. Springer; New York: 2015. p. 218
6. Pawley, JB., editor. Handbook of Biological Confocal Microscopy. Plenum Press; New York: 1995. p. 632
7. Huang B, Bates M, Zhuang X. Super resolution fluorescence microscopy. Annu Rev Biochem. 2009; 78:993–1016. [PubMed: 19489737]
8. Schermelleh L, Heintzmann R, Leonhardt H. A guide to super-resolution fluorescence microscopy. JCB. 2010; 190(2):165–175. [PubMed: 20643879]
9. Hell SW. Microscopy and its focal switch. Nature Methods. 2009; 6:24–32. [PubMed: 19116611]
10. Huang B, Wang W, Bates M, Zhuang X. Three-dimensional super-resolution imaging by stochastic optical reconstruction microscopy. Science. 2008; 319:810–813. [PubMed: 18174397]
11. Pantanowitz L, Valenstein PN, Evans AJ, Kaplan KJ, Pfeifer JD, Wilbur DC, Collins LC, Colgan TJ. Review of the current state of whole slide imaging in pathology. J Pathol Inform. 2015; 2:36.
12. Ji N. The practical and fundamental limits of optical imaging in mammalian brains. Neuron. 2014; 83:1242–1245. [PubMed: 25233304]
13. Garaschuk O, Milos R-I, Konnerth A. Targeted bulk-loading of fluorescent indicators for two-photon brain imaging in vivo. Nature Protocols. 2006; 1(1):380–386. [PubMed: 17406260]
14. Jung JC, Mehta AD, Aksay E, Stepnoski R, Schnitzer MJ. In vivo mammalian brain imaging using one- and two-photon fluorescence microscopy. J Neurophysiol. 2004; 92:3121–3133. [PubMed: 15128753]
15. Saleh, BEA., Teich, MC. Fundamentals of Photonics. 2. Wiley-Interscience; 2007. p. 1177
16. Joannopoulos, JD., Johnson, SG., Winn, JN., Meade, RD. Photonic Crystals Molding the Flow of Light. Princeton University Press; 2008. p. 286
17. Polo, JA., Mackay, TG., Lakhtakia, A. Electromagnetic Surface Waves A Modern Perspective. Elsevier; New York: 2013. p. 293
18. Badugu R, Nowaczyk K, Descrovi E, Lakowicz JR. Radiative decay engineering 6: Fluorescence one-dimensional photonic crystals. Analy Biochem. 2013; 442:83–96.
19. Shilkin, Da, Lyubin, EV., Soboleva, IV., Fedyanin, Aa. Direct measurements of forces induced by Bloch surface waves In a one-dimensional photonic crystal. Opt Letts. 2015; 40:4883–4886. [PubMed: 26512474]

20. Novotny, L., Hecht, B. Principles of Nano-Optics. Cambride Press; 2006. p. 539
21. Markel, VA., George, TF. Optics of Nanostructured Materials. John Wiley & Sons; New York: 2001. p. 553
22. Lakowicz JR, Ray K, Chowdhury M, Szmacinski H, Fu Y, Zhang J, Nowaczyk N. Plasmon-controlled fluorescence: a new paradigm in fluorescence spectroscopy. Analyst. 2008; 133:1308–1346. [PubMed: 18810279]
23. Deng W, Goldys EM. Plasmonic approach to enhanced fluorescence for applications in biotechnology and the life sciences. Langmuir. 2012; 28:10152–10163. [PubMed: 22568517]
24. Fort E, Gresillon S. Surface enhanced fluorescence. J Phys D Appl Phys. 2008; 41:013001–013032.
25. Giannini V, Fernanedez-Dominguez AI, Heck SC, Maier SA. Plasmonic nanoantennas: Fundamentals and their use in controlling the radiative properties of nanoemitters. Chem Rev. 2011; 111:3888–3912. [PubMed: 21434605]
26. Cao S-H, Cai W-P, Liu Q, Li Y-Q. Surface plasmon-coupled emission: What can directional emission bring to the analytical sciences? Annu Rev Chem. 2012; 5:317–336.
27. Calander N. Theory and simulation of surface plasmon-coupled directional emission from fluorophores at planar structures. Anal Chem. 2004; 76(8):2168–2173. [PubMed: 15080724]
28. Lakowicz JR. Radiative decay engineering 3. Surface plasmon-coupled directional emission. Anal Biochem. 2004; 324:153–169. [PubMed: 14690679]
29. Aouani H, Mahboub O, Bonod N, Devaux E, Popov E, Rigneault H, Ebbesen TW, Wenger J. Bright unidirectional fluorescence emission of molecules in a nanoaperture with plasmonic corrugations. Nano Letts. 2011; 11:637–644. [PubMed: 21247202]
30. Harats MG, Livneh N, Zaiats G, Youchelis S, Paltiel Y, Lifshitz E, Rapaport R. Full spectral and angular characterization of highly directional emission from nanocrystal quantum dots positioned on circular plasmonic lens. Nano Letts. 2014; 14:4766–5771.
31. Durnin J. Exact solutions for nondiffracting beams. I. The scalar theory. J Opt Soc Am A. 1987; 4:651–654.
32. Durnin J, Miceli JJ, Eberly JH. Diffraction-Free Beams. Phys Rev Lett. 1987; 58:1499–1501. [PubMed: 10034453]
33. Born, M., Wolf, E. Principles of Optics. Cambridge University Press; 2002. p. 952
34. Klein, MV. Optics. John Wiley & Sons; New York: 1970. p. 647
35. McGloin D, Dholakia K. Bessel beams: diffraction in a new light. Contemp Phys. 2005; 46:15–28.
36. McQueen CA, Arlt J, Dholakia K. An experiment to study a “nondiffracting” light beam. Am J Phys. 1999; 67:912–915.
37. Brzobohaty O, Clzmar T, Zemanek P. High quality quasi-Bessel beam generated by round-tip axicon. Opt Exp. 2008; 16:12688–12700.
38. Milne G, Jeffries GDM, Chiu DT. Tunable generation of Bessel beams with a fluidic axicon. Appl Phys Lett. 2008; 92:261101. [PubMed: 19529839]
39. Vasara A, Turunen J, Friberg AT. Realization of general nondiffracting beams with computer-generated holograms. J Opt Soc Am A. 1989; 6:1748–1754. [PubMed: 2585173]
40. Davis JA, Carcole E, Cottrell DM. Nondiffracting interference patterns generated with programmable spatial light modulators. Appl Opt. 1996; 35:599–602. [PubMed: 21069044]
41. Davis JA, Carcole E, Cottrell DM. Intensity and phase measurements of Nondiffracting beams generated with a magneto-optic spatial light modulator. Appl Opt. 1996; 35:593–598. [PubMed: 21069043]
42. Zhang, Douguo, Yuan, Xiaocong, Bouhelier, Alexandre. Direct image of surface-plasmon-coupled emission by leakage radiation microscopy. Appl Opt. 2010; 49:875. [PubMed: 20154755]
43. Tang WT, Chung E, Kim YH, So PT, Sheppard CJ. Investigation of the point spread function of surface plasmon-coupled emission microscopy. Opt Express. 2007; 15:4634–4646. [PubMed: 19532709]
44. Tang WT, Chung E, Kim Y-H, So PT, Sheppard CJR. Surface-plasmon-coupled emission microscopy with a spiral phase plate. Opt Lett. 2010; 35:517. [PubMed: 20160803]

45. Zhang Q. Cylindrical vector beams: from mathematical concepts to applications. Adv Opt Phot. 2009; 1:1–57.
46. Hamrle J, Micaiah BD. Theory of the radiation of dipoles placed within a multilayer system. Appl Opt. 2000; 39:3968–3977. [PubMed: 18349977]
47. Torok P, Higdon PD, Wilson T. Theory for confocal and conventional microscopes imaging small dielectric scatters. J Mod Opt. 1998; 45:1681–1698.
48. Richards B, Wolf E. Electromagnetic diffraction in optical systems. II. Structure of the image field in an aplanatic system. Proc Roy Soc (London) A. 1959; 253:358–379.
49. Indebetouw G. Nondiffracting optical fields: some remarks on their analysis and synthesis. J Opt Soc Am A. 1989; 6:150–152.
50. Planchon TA, Gao L, Milkie DE, Davidson MW, Galbraith JA, Gallbraith CG, Betzig E. Rapid three-dimensional isotropic imaging of living cells using Bessel beam plane illumination. Nature Methods. 2011; 8:417–423. [PubMed: 21378978]
51. McGloin D, Dholakia K. Bessel beams: diffraction in a new light. Contemp Phys. 2005; 46:15–28.
52. Fan D, Wang L, Ekinci Y. Nanolithogrphy using Bessel beams of extreme ultraviolet wavelength. Sci Rep. 2016; 6:31301–1/8. [PubMed: 27501749]
53. Garces-Chavez V, McDloin D, Metville H, Sibbett W, Dholakia K. Simultaneous micromanipulation in multiple planes using a self-reconstructing light beam. Nature. 2002; 419:14–147.
54. Arlt J, Garces-Chavez V, Sibbett W, Dholakia K. Optical micromanipulation using a bessel light beam. Opt Commun. 2001; 197:239–245.
55. Arlt J, Garces-Chavez V, Sibbett W, Dholakia K. Optical micromanipulation using a Bessel light beam. Optics Commun. 2001; 197:239–245.
56. Chremmos ID, Chen Z, Christodoulides DN, Efremidis NK. Bessel-like optical beams with arbitrary trajectories. Optics Letters. 2012; 37(23):5003–5005. [PubMed: 23202118]
57. Zhang P, Wang S, Liu Y, Yin X, Lu C, Chen Z, Zhang X. Plasmonic airy beams with dynamically controlled trajectories. Optics Letters. 2011; 36(16):3191–3913. [PubMed: 21847204]
58. Fahrbach FO, Rohrbach A. Propagation stability of self-reconstructing Bessel beams enables contrast-enhanced imaging in thick media. Nature Commun. 2011; 632:1–8.
59. Garces-Chavez V, McGloin D, Melville H, Sibbett W, Dholakia K. Simultaneous micromanipulation in multiple planes using a self-reconstructing light beam. Letts Nature. 2002; 419:145–147.
60. Fahrbach FO, Simon P, Rohrbach A. Microscopy with self-reconstructing beams. Nature Photonics. 4:780–785.
61. Purnapatra SB, Bera S, Mondal PP. Spatial filter based Bessel-like beam for improved penetration depth imaging in fluorescence microscopy. Sci Rep. 2012; 692:1–11.
62. Fahrbach FO, Rohrbach A. Propagation stability of self-reconstructing Bessel beams enables contrast-enhanced imaging in thick media. Nature Communcations. 3:632-1/8.

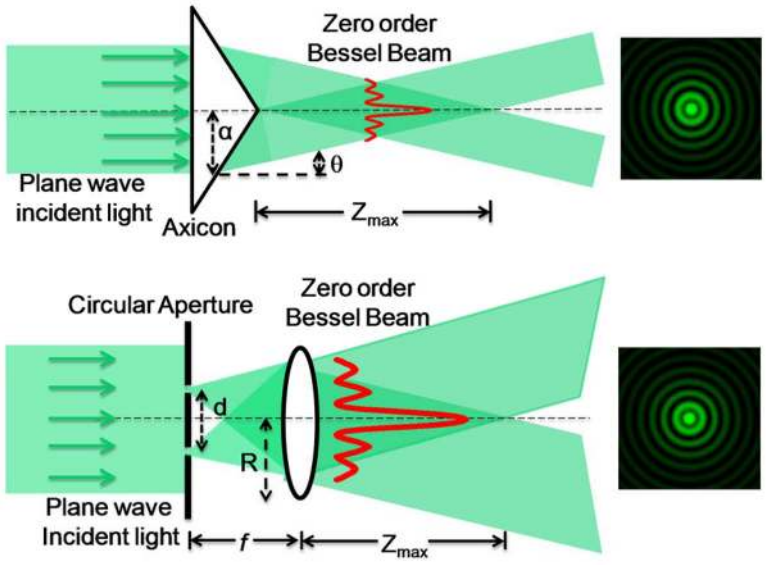

Figure 1.

Formation of a Bessel beam with a plane wave incident light and an axicon (top) and a circular aperture in an opaque mask (bottom). The right side images show the transverse profiles of zero order Bessel Beams formed using these methods.

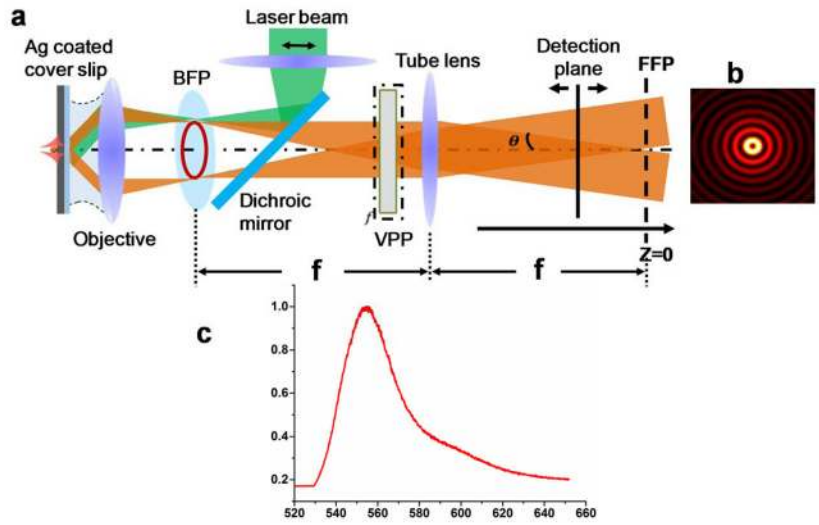

Figure 2.

Experimentally generation of non-diffracting fluorescence. (a) Schematic configuration of experimental setup. FPS, fluorescent polystyrene sphere, BFP, back focal plane; VPP, vortex phase plate; FFP, front focal plane; f, focal length of the tube lens. BFP represents the back focal plane of the objective, which is consistent with the front focal plane of the tube lens. FFP represent the front focal plane (or imaging plane) of the system, it is also the back focal plane of the tube lens. A VPP can be inserted into the optical path to convert the first order Bessel like Beam to zeroth-order. (b) The transverse profile image shows the first order Bessel Beams formation. (c) Fluorescence spectrum of the fluorescent bead with a diameter at 40 nm. The spectrum peak is located at 555 nm.

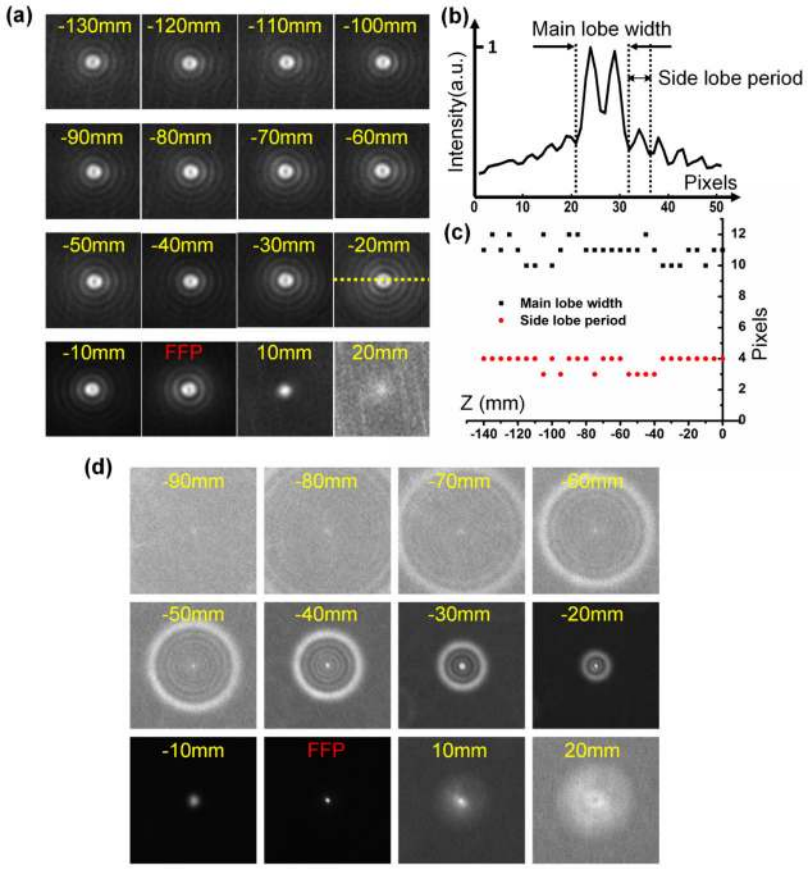

Figure 3.

Fluorescence Bessel-like beam of the first order. (a) Transvers intensity distribution at different Z positions as labeled in each image. The number of pixels of each image is 51 by 51. The pixel size is 6.5 μm. (b) Normalized cross section profile of transvers intensity at position Z = −20 mm along the dashed line. (c) Main lobe width and side lobe period of transvers intensity distribution at different Z position with 5 mm step. (d) Transvers intensity distribution at different Z positions when the FPS bead was on a glass substrate without Ag film. The number of pixels of each image is 200 by 200.

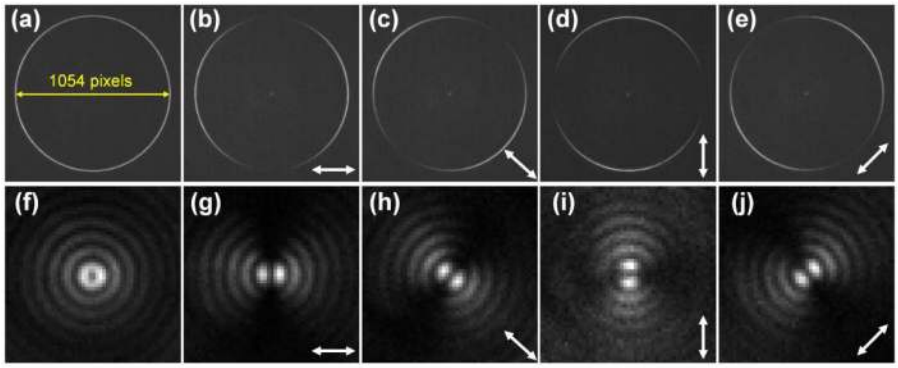

Figure 4.

Polarization state of the fluorescence. (a) Back focal plane (BFP) image of emission from the fluorescent bead. (b), (c), (d) and (e) BFP images with a linear polarizer placed before the detector. The double headed arrow in each panel indicates the orientation of the polarizer. (f), (g), (h), (i) and (j), are the corresponding transverse intensity distribution of fluorescence images at Z= −20 mm.

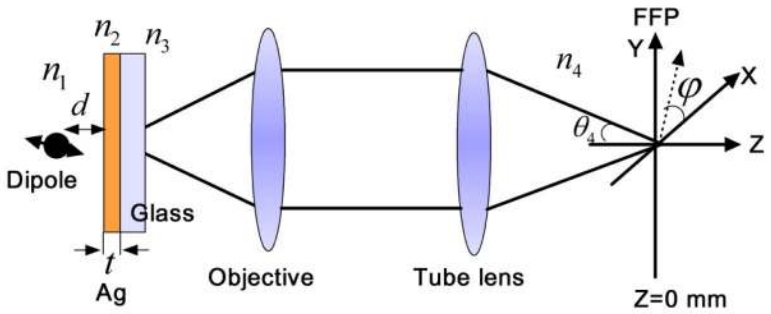

Figure 5.

A schematic diagram of the surface Plasmon mediated fluorescence imaging process within a 4 f optical system. *d* represents the distance between the dipole and the silver film. n1, n2, n3, and n4 represent the refractive index of the air, silver, glass substrate and the medium in image space (after the tube lens). The left lens is the objective and the right one is the tube lens.

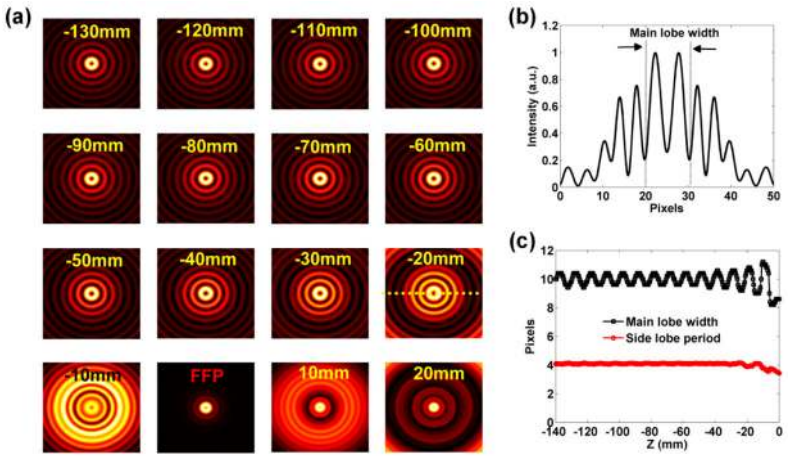

Figure 6.

Calculated first-order fluorescence Bessel-like beam. (a) Transverse intensity distribution at different Z. The number of pixels of each image is 51 by 51. The pixel size is 6.5 μm. (b) Normalized cross section profile of transverse intensity at position Z = −20 mm along the dashed line. (c) Main lobe width and side lobe period of transverse intensity distribution at different Z positions with 5mm step.

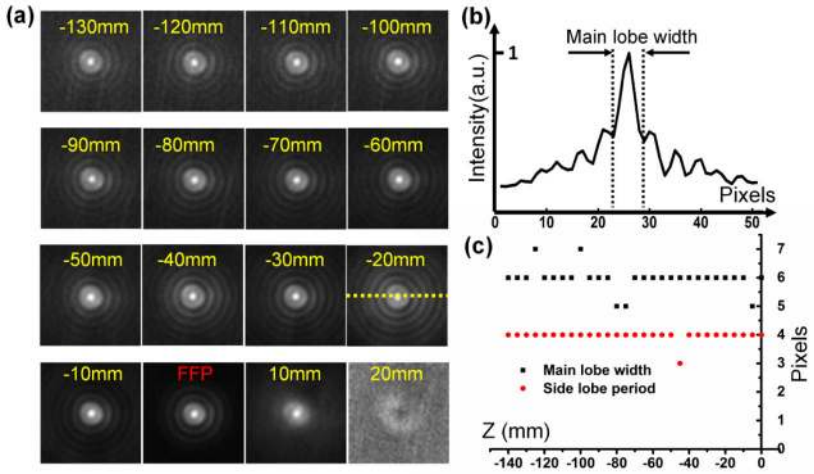

Figure 7.

Non-diffracting fluorescence of the zeroth-order. (a) Transvers intensity distribution at different Z positions as labeled in each image. The number of pixels of each image is 51 by 51. The pixel size is 6.5 μm. (b) Normalized cross section profile of transvers intensity at Z position = −20mm. (c) Main lobe width and side lobe period of transvers intensity distribution at different Z positions with 5 mm step.

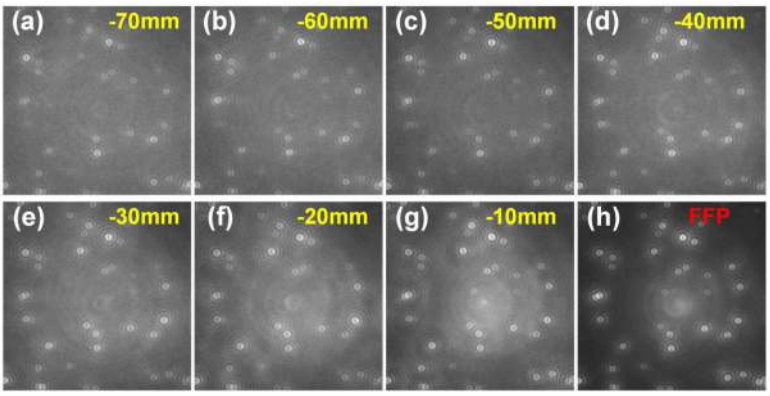

Figure 8.

Simultaneous generation of multiple diffraction free beams. (a)–(h), recorded fluorescence intensity at different Z positions. The number of pixels of each image is 200 by 200. The pixel size is 6.5 μm.